C. Bassi, A. Abbà, L. Bonaventura, L. Valdettaro
Large Eddy Simulation of non-Boussinesq gravity currents with a DG Method
Theoretical and Computational Fluid Dynamics, Vol. 34, 2020, p. 231-247
doi:10.1007/s00162-020-00525-z

Noname manuscript No.
(will be inserted by the editor)

Large Eddy Simulation of non-Boussinesq gravity currents with a DG method

Caterina Bassi · Antonella Abbà · Luca Bonaventura · Lorenzo Valdettaro

Received: date / Accepted: date

Abstract We present results of three-dimensional Direct Numerical Simulations (DNS) and Large Eddy Simulations (LES) of turbulent gravity currents with a Discontinuous Galerkin (DG) Finite Elements method. In particular, we consider the lock-exchange test case as a benchmark for gravity currents. Since, to the best of our knowledge, non-Boussinesq three-dimensional reference DNS are not available in the literature for this test case, we first perform a DNS experiment. The DNS provides an accurate description of the turbulent phenomena and highlights some differences with respect to the Boussinesq regime, like the non-symmetric pattern in the evolution of instabilities at the interfacial region and the fact that less turbulent structures are present due to greater stratification. A periodic pattern is also evident in the time evolution of turbulent mixing. The DNS is then employed to assess the performance of different LES models. In particular, we have considered the isotropic dynamic model and an anisotropic dynamic model. The LES results provide a first indication about the superiority of dynamic models with respect to no-model

C. Bassi
MOX Modelling and Scientific Computing, Dipartimento di Matematica, Politecnico di Milano, Via Bonardi 9, 20133 Milano, Italy.
E-mail: caterina.bassi@polimi.it

Antonella Abbà
Dipartimento di Scienze e Tecnologie Aerospaziali, Politecnico di Milano, Via La Masa 34, 20156 Milano, Italy.

Luca Bonaventura
MOX Modelling and Scientific Computing, Dipartimento di Matematica, Politecnico di Milano, Via Bonardi 9, 20133 Milano, Italy.

Lorenzo Valdettaro
MOX Modelling and Scientific Computing, Dipartimento di Matematica, Politecnico di Milano, Via Bonardi 9, 20133 Milano, Italy.

LES. However, the considered Reynolds numbers in the non-Boussinesq context are still too low to draw firm conclusions about the superiority of the present explicit LES approach with respect to an implicit LES approach.

Keywords Direct Numerical Simulation · Large Eddy Simulation · Dynamical models · Density currents · Discontinuous Galerkin method

1 Introduction

Gravity currents, arising when a heavier fluid propagates into a lighter one in a predominantly horizontal direction, are very common in geophysical flows. In atmospheric gravity currents, the density difference is typically caused by the temperature difference between the cold front and the warmer surrounding air. In oceanic flows, density differences are caused instead by salinity and temperature gradients, while in pyroclastic flows the density difference is due to the presence of suspended particles in the flow. A comprehensive description of environmental gravity currents can be found e.g. in [25]. For small density differences, density variations in the momentum equation can be neglected in the inertia term, but retained in the buoyancy term, yielding the so called Boussinesq approximation, see e.g. [15]. This approximation has been employed in most experimental and computational studies of gravity currents reported in the literature, see e.g. [4,16,21,22]. However, in several of the above listed phenomena, non-Boussinesq effects become important.

Gravity currents appear to be a particularly interesting phenomenon from the point of view of turbulence modelling, since a wide range of interesting phenomena arise, such as breaking internal waves and Kelvin-Helmholtz instabilities.

The main purpose of the present work is to present the first DNS results for a gravity current benchmark in the non-Boussinesq regime and to assess the performance of different LES turbulence models in the same setting. We expect that the stronger density variations in this regime provide a more appropriate framework for the validation of LES models that have been traditionally developed under constant density assumptions, see the discussion in [13]. More specifically, a three-dimensional lock exchange problem, similar to that studied in [21] in the framework of the Boussinesq approximation, was extended to the non-Boussinesq regime. With respect to the two-dimensional DNS already present in the literature, see e.g. [5], the three-dimensional DNS allows to effectively capture the vortex stretching and the loss of coherence of the three-dimensional coherent structures, providing more insight in the turbulent phenomena arising in gravity currents. Moreover the three-dimensional DNS highlights some differences with respect to the Boussinesq results, like the non-symmetric pattern in the evolution of the instabilities at the interfacial region between heavy and light fluids and the presence of far less turbulent structures due to the greater stratification. The DNS results have then been employed for the assessment of different subgrid LES models, the more conventional isotropic dynamic model [14] and the less conventional anisotropic

dynamic model [2] together with the standard Smagorisnky model, with respect to an implicit LES approach. The LES results provide a first indication about the superiority of the dynamic models with respect to the no-model LES. Concerning the Smagorinsky model and as it is well known, results similar to the results obtained employing dynamic models can be obtained only by carefully choosing the value of the Smagorinsky constant. Notice, however, that the considered Reynolds numbers in the present non-Boussinesq regime do not allow to reach a firm conclusion about the advantage of introducing explicit LES models with respect to an implicit LES approach.

The numerical framework chosen to implement the models is that of a Discontinuous Galerkin discretization. Such a framework allows to generalize the concept of LES filter as a projection onto the polynomial space related to the discretization, thus making it possible to apply it to arbitrary unstructured meshes. This is conceptually similar to what is done in Variational Multi-Scale (VMS) models, see e.g. [17,19].

The paper is organized as follows. Section 2 provides a brief introduction of the mathematical and numerical model employed for the treatment of turbulent gravity currents, while for a more detailed description of the different subgrid turbulence models and of the Discontinuous Galerkin method we refer to [1]. The set-up of the DNS and LES experiments is described in section 3. The DNS results are discussed in section 4, while the LES are presented in section 5 and their quality assessed in terms of the corresponding DNS. Some conclusions and perspectives for future work are presented in section 6.

2 The mathematical and numerical model

The mathematical model we employ for the description of gravity currents is based on the compressible Navier-Stokes equations, filtered with the same procedure as in [1,8]. The filtering operator, which is denoted by $\overline{\cdot}$, is defined as the projection onto a space of piecewise polynomial functions of the same degree p of the piecewise polynomial basis functions used by the DG method. The filter is as a consequence in-built in the DG discretization approach. The choice of p implicitly defines a spatial filter scale Δ, whose full definition is given in [1]. In the same paper, the non commutativity of this filter with the continuous differential operators is also discussed. An analysis of the commutation error of a similar approach can be found in [6].

The Favre filter operator $\widetilde{\cdot}$ (see e.g. [11]) is then defined implicitly by the Favre decomposition, which is given for a generic function f by

$$\overline{\rho f} = \overline{\rho}\widetilde{f}. \tag{1}$$

The non-dimensionalization of the Navier-Stokes equations in conservation form is performed as in [7,8], resulting in the following non-dimensional version

of the equations:

$$\partial_t \overline{\rho} + \partial_j(\overline{\rho}\widetilde{u}_j) = 0 \tag{2a}$$

$$\partial_t\left(\overline{\rho}\widetilde{u}_i\right) + \partial_j\left(\overline{\rho}\widetilde{u}_i\widetilde{u}_j\right) + \partial_i\overline{p} - \partial_j\widetilde{\sigma}_{ij} = -\partial_j\tau_{ij} + \overline{\rho}f_i \tag{2b}$$

$$\begin{aligned}\partial_t\left(\overline{\rho}\widetilde{e}\right) + \partial_j\left(\overline{\rho}\widetilde{h}\widetilde{u}_j\right) - \partial_j\left(\widetilde{u}_i\widetilde{\sigma}_{ij}\right) + \partial_j\widetilde{q}_j \\ = -\frac{1}{(\gamma-1)Ma^2}\partial_j Q_j^{\mathrm{sgs}} - \frac{1}{2}\partial_j\left(J_j^{\mathrm{sgs}} - \tau_{kk}\widetilde{u}_j\right) + \overline{\rho}f_j\widetilde{u}_j,\end{aligned} \tag{2c}$$

where the Einstein summation convention has been employed. Notice that $\overline{\rho}$, $\overline{\rho}\widetilde{u}_i$ and $\overline{\rho}\widetilde{e}$ are the filtered density, the filtered components of the momentum and the filtered total energy, respectively, while $\widetilde{h}$ is the filtered specific enthalpy defined as $\widetilde{h} = \widetilde{e} + \overline{p}/\overline{\rho}$. $\widetilde{\sigma}_{ij}$ and $\widetilde{q}_i$ are the filtered diffusive fluxes, for which the following expressions are assumed:

$$\widetilde{\sigma}_{ij} = \mu\widetilde{\mathcal{S}}_{ij}^d, \qquad \widetilde{q}_i = -\lambda\partial_i\widetilde{T}, \tag{3}$$

where the non-dimensional dynamic viscosity μ is given by the Sutherland law as in [7] while the thermal conductivity λ is given by $\lambda = \mu c_p/Pr$, with c_p non-dimensional specific heat at constant pressure and Pr Prandtl number (see [7] and [1]). $\widetilde{\mathcal{S}}_{ij} = \partial_j\widetilde{u}_i + \partial_i\widetilde{u}_j$ is the strain rate, while $\widetilde{\mathcal{S}}_{ij}^d = \widetilde{\mathcal{S}}_{ij} - \frac{1}{3}\widetilde{\mathcal{S}}_{kk}\delta_{ij}$ is its the deviatoric part. Notice that Ma is the Mach number. The gravity forcing term is given by $\mathbf{f} = (0, 0, -1/Fr^2)$, where Fr is the Froude number, whose expression is specified in equation (8). τ_{ij}, Q_j^{sgs} and J_j^{sgs} are the subgrid stress tensor, the subgrid temperature flux and the subgrid turbulent diffusion flux, respectively, whose expressions are:

$$\tau_{ij} = \overline{\rho u_i u_j} - \overline{\rho}\widetilde{u}_i\widetilde{u}_j, \tag{4a}$$

$$Q_i^{\mathrm{sgs}} = \overline{\rho u_i T} - \overline{\rho}\widetilde{u}_i\widetilde{T} = \overline{\rho}\left(\widetilde{u_i T} - \widetilde{u}_i\widetilde{T}\right), \tag{4b}$$

$$\begin{aligned}J_i^{\mathrm{sgs}} &= \overline{\rho u_i u_k u_k} - \overline{\rho}\widetilde{u}_i\widetilde{u}_k\widetilde{u}_k = \overline{\rho}\widetilde{u_i u_k u_k} - \overline{\rho}\widetilde{u}_i\widetilde{u}_k\widetilde{u}_k \\ &= \tau(u_i, u_k, u_k) + 2\widetilde{u}_k\tau_{ik} + \widetilde{u}_i\tau_{kk}.\end{aligned} \tag{4c}$$

In the last equality of equation (4c), the generalized central moments $\tau(u_i, u_j, u_k) = \overline{\rho}\widetilde{u_i u_j u_k} - \widetilde{u}_i\tau_{jk} - \widetilde{u}_j\tau_{ik} - \widetilde{u}_k\tau_{ij} - \overline{\rho}\widetilde{u}_i\widetilde{u}_j\widetilde{u}_k$ (see [12]) have been introduced.

These subgrid terms just introduced need modeling. In this work, we have employed the Smagorinsky model [26], the isotropic dynamic model [14] and the anisotropic dynamic model proposed in [2]. For the anisotropic dynamic model the closure relations for the terms (4a), (4b) and (4c) are the following:

$$\tau_{ij} = -\overline{\rho}\Delta^2|\widetilde{\mathcal{S}}|\mathcal{B}_{ijrs}\widetilde{\mathcal{S}}_{rs}, \tag{5a}$$

$$Q_i^{\mathrm{sgs}} = -\overline{\rho}\Delta^2|\widetilde{\mathcal{S}}|\mathcal{B}_{ir}^Q\partial_r\widetilde{T}, \tag{5b}$$

$$J_i^{\mathrm{sgs}} = -\overline{\rho}\Delta^2|\widetilde{\mathcal{S}}|\mathcal{B}_{ir}^J\partial_r\left(\frac{1}{2}\widetilde{u}_k\widetilde{u}_k\right) + 2\widetilde{u}_k\tau_{ik} + \widetilde{u}_i\tau_{kk}, \tag{5c}$$

where Δ is the filter scale, $|\widetilde{\mathcal{S}}| = \sqrt{\widetilde{\mathcal{S}}_{ij}\widetilde{\mathcal{S}}_{ij}/2}$, $\mathcal{B}_{ijrs}$, $\mathcal{B}^{Q}_{ir}$ and $\mathcal{B}^{J}_{ir}$ are tensors and are dynamically computed following the procedure described in [1]. Similar expressions hold for the isotropic dynamic model, with the difference that, for the subgrid stress tensor in the momentum equation, the deviatoric and isotropic part are modeled separately and that all dynamic constants assume scalar values. For a more complete and detailed description of subgrid models we refer to [1].

Concerning the numerical discretization, the Discontinuous Galerkin approach we employ is based on that presented and fully tested in [1,8,30]. The numerical fluxes, which are responsible for the coupling between elements, are computed with the well known exact Godunov Riemann solver for the convective part [28] and with the Local Discontinuous Galerkin method for the viscous part (see [3,9]). We have used as basis functions piecewise polynomials of degree $p = 4$. The quadrature formulae employed for the numerical integration are exact for polynomial degrees up to $2p$: this guarantees the exact integration of the mass matrix but is insufficient for the exact integration of the convective flux terms. In order to avoid severe aliasing errors we have used the so called polynomial de-aliasing procedure, first introduced in [20]. The numerical quadrature precision has been increased such that the aliasing errors due to the convective flux integrals are reduced and it is possible, as a consequence, to obtain stable simulations. In our case a number of integration points corresponding to exact integration of polynomials of degree 12 has been employed.

For the time discretization, a fourth order accurate, Strong Stability Preserving explicit Runge-Kutta method, see e.g. [27], has been employed for all the simulations.

3 Set-up of the numerical experiments and definition of diagnostic quantities

We have carried out the DNS and the LES of a three-dimensional lock exchange problem at two different Reynolds numbers ($Re = 3000$ and $Re = 6000$). In the lock exchange problem a membrane initially divides the domain in two compartments. In our case the two chambers are filled with the same fluid at different densities on the two sides of the membrane (higher density on the left and lower density on the right). Upon the removal of the membrane, the dense front moves rightward along the lower boundary, while the light front propagates leftward along the upper boundary. At the interfacial region there is the development of instabilities due to the velocity difference and the shear. The experimental setting of [21] is followed for the definition of the domain and the initial and boundary conditions. Notice that, however, we have considered a density ratio $\gamma_r = 0.7$. Thus a non-Boussinesq regime has been explored, contrary to what was done in [21], where simulations in the Boussinesq regime were carried out. The stronger density variations in this regime should provide a more appropriate framework for the validation

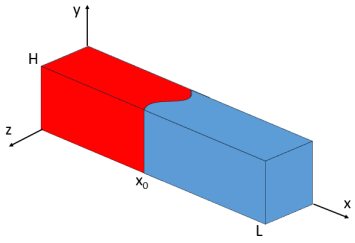

Fig. 1: Initial density datum for the lock-exchange test case.

of LES models that have been traditionally developed under constant density assumptions. The Reynolds number is defined as $Re = (u_b^* H^* \rho_1^*)/\mu_0^*$, where H^* is the height of the domain, ρ_1^* is the higher density, μ_0^* is the dynamic viscosity, while u_b^* is the buoyancy velocity defined as follows:

$$u_b^* = \sqrt{\frac{g^*(\rho_1^* - \rho_2^*)H^*}{\rho_1^*}}, \tag{6}$$

with $\rho_1^* > \rho_2^*$. Notice that the symbol * identifies dimensional quantities.

The initial condition is presented in figure 1. The domain length is $L = 5$, its height is $H = 1$, its width is $W = 1$, while the position of the initial discontinuity is $x_0 = 2.5$. The initial density datum is characterized by a sharp transition layer. Moreover, a perturbation is applied in the spanwise direction in order to ease the transition to turbulence, so that

$$\rho_0(x,y,z) = \begin{cases} 1 & \text{if } 0 \le x < a \\ 1 + 100(\gamma_r - 1)(x/L - 0.495 + \eta) & \text{if } a \le x < b \\ \gamma_r & \text{if } b \le x \le L, \end{cases}$$

where $a = L/2 - (0.005 + \eta)L$, $b = L/2 + (0.005 - \eta)L$ and $\eta = 0.05\sin(2\pi\frac{z}{W})$.

The initial pressure at the top of the domain is defined as in [8]:

$$p_{init}^{top} = \frac{1}{\gamma Ma^2}, \tag{7}$$

where γ is the ratio between the specific heats and $Ma = 0.1$. An hydrostatic pressure profile is assumed in the rest of the domain. The initial temperature profile is computed from density and pressure using the equation of state for ideal gases, while the initial velocity is equal to zero in the whole domain. According to the non-dimensionalization employed in the present work (which is the same as in [7,8]), the Froude number can be expressed as:

$$Fr = \sqrt{1 - \gamma_r}. \tag{8}$$

We employ slip boundary conditions in the streamwise (x) and vertical (y) directions , while periodic boundary conditions are imposed in the spanwise direction (z).

Equations (2) are integrated until $T_{fin} = 60$ non-dimensional time units. As a consequence our simulations are shorter than those in [21], where a final time $T_{fin} = 110$ is reached. The final simulation time we choose is a compromise between the computational cost and the fact that $T_{fin} = 60$ is a time for which, in the Boussinesq simulations in [21], apparent differences are present between DNS and LES. It will be also shown that the considered final time is sufficient to reach a flow regime in which turbulent mixing is considerably reduced with respect to the initial vigorous activity.

In order to analyze quantitatively the DNS results and to assess the ability of the different LES models in reproducing them, various diagnostic quantities have been considered. The temporal evolution of the dissipated energy was computed integrating in time the following equation:

$$\frac{dE_d}{dt} = \int_\Omega \left\{ \overline{\rho}\nu \left[\frac{1}{2}(\partial_j \widetilde{u}_i + \partial_i \widetilde{u}_j)^2 - \frac{2}{3}(\nabla \cdot \widetilde{\mathbf{u}})^2 \right] - \tau_{ij}\partial_j \widetilde{u}_i \right\} d\mathbf{x}, \tag{9}$$

where the first contribution accounts for kinetic energy dissipation due to viscous terms, while the second contribution accounts for energy dissipation due to turbulent terms.

The second diagnostic quantity we have considered is the time evolution of the Reference Potential Energy (RPE). This quantity, which has been first introduced in [31], corresponds to the minimum potential energy that can be obtained through an adiabatic redistribution of the fluid. Starting from the potential energy E_p and the reference potential energy RPE, we can compute the available potential energy (APE) as:

$$APE(t) = E_p(t) - RPE(t). \tag{10}$$

As discussed in [31], the APE is the part of the potential energy that can actually be transferred to kinetic energy because of the turbulent mixing.

As pointed out in [31] and recalled in [21], the reference potential energy increases with time, thanks to the stratified mixing: the RPE is, as a consequence, an effective measure of how much mixing has occurred in the fluid. We have computed the RPE following the procedure outlined in [29]. We have introduced the density variable $\tilde{\rho}$ in the sample space $[\rho_m, \rho_M]$, with ρ_m and ρ_M minimum and maximum densities, respectively. The probability of density ρ to be in the interval $[\tilde{\rho}, \tilde{\rho} + d\tilde{\rho}]$ is denoted by $P(\tilde{\rho})d\tilde{\rho}$, where $P(\tilde{\rho})$ is a probability density function. This function is estimated in practice dividing the density interval $[\rho_m, \rho_M]$ into different bins. The density field is then scanned and, for each element, we consider the density value in each Gauss integration point. If the value falls into a particular bin, a quantity equal to the Gauss weight associated with the Gauss point is accounted for that bin. The probability density function is then obtained normalizing the volume contained in each bin by the volume of the whole domain, after the completion of the whole scanning procedure. We have also tried to compute the probability density function employing the element averaged values for the density. Since no difference was present in the RPE, we concluded that the choice of the points does not have a significant impact on the RPE evaluation.

The quantity $Z_r(\rho)$ is the height of the fluid of density ρ in the minimum potential energy state, while dZ_r is the thickness of the layer containing fluid of density between $\tilde{\rho}$ and $\tilde{\rho}+d\tilde{\rho}$. If the layers have the same horizontal surface A, the volume occupied by this layer of fluid is:

$$AdZ_r|_\rho = |\Omega|P(\tilde{\rho})d\tilde{\rho}|_\rho.$$

This equation is then integrated over $\tilde{\rho}$ in order to obtain the profile $Z_r(\rho)$:

$$Z_r(\rho) = H\int_\rho^{\rho_M} P(\tilde{\rho})d\tilde{\rho}. \tag{11}$$

Since the RPE is defined as the potential energy of the reference state, whose vertical profile is given by equation (11), the following equation was employed for its computation:

$$RPE = \frac{1}{Fr^2}LW\int_0^H \rho(Z_r)Z_r dZ_r, \tag{12}$$

where $\rho(Z_r)$ is the reference density expressed as a function of the reference coordinate Z_r. In order to make comparisons with the Boussinesq results in [21], the results will be presented in terms of the following normalized RPE:

$$\Delta RPE = \frac{RPE - RPE0}{RPE0}, \tag{13}$$

where $RPE0$ is the Reference Potential Energy at the beginning of the simulation.

We have also compared the results of the different simulations in terms of instantaneous fields at different instants of time. We have considered in particular density fields and $Q-$criterion fields. This criterion has been introduced in [18] by identifying a vortex as a spatial region where the Euclidean norm of the vorticity tensor dominates that of the strain rate, i.e.:

$$Q = \frac{1}{2}\left(\frac{1}{4}|\Omega|^2 - \frac{1}{4}|\mathcal{S}^d|^2\right) > 0, \tag{14}$$

where $\mathcal{S}^d_{ij} = \partial_j u_i + \partial_i u_j - \frac{1}{3}(2\partial_k u_k)\delta_{ij}$ and $\Omega_{ij} = \partial_j u_i - \partial_i u_j$. Notice that the $Q-$criterion allows to distinguish between pure shearing motion and the actual swirling motion of a vortex.

In addition to the instantaneous fields just mentioned, we evaluate also Turbulent Kinetic Energy (TKE), turbulent stresses and mean velocity profiles. Since the lock-exchange test case is non-stationary and has only one homogeneity direction, z, we perform the averaging procedure only along the z direction, thus obtaining statistics which change in time and which depend upon the value of the coordinates x and y. We will represent in particular the profiles of the statistics along the y direction and at fixed values for time and x coordinate.

Table 1: Number of DOFs associated to the DNS, to the DNS50 and to the LES.

	$Re = 3000$	$Re = 6000$
DNS	3800000	3800000
DNS50	1900000	1900000
LES	80000	300000

4 Results of the DNS experiments

In this section, the main results obtained from the DNS experiments are presented, to be compared in the following section with the corresponding LES results.

The computational grid for our computations is built starting from a structured hexahedral mesh. Each hexahedron is divided into N_t tetrahedra. The expressions for the equivalent grid spacings are:

$$\Delta_x = \frac{L}{N_x \sqrt[3]{N_t N_p}}, \quad \Delta_y = \frac{W}{N_y \sqrt[3]{N_t N_p}}, \quad \Delta_z = \frac{H}{N_z \sqrt[3]{N_t N_p}}, \tag{15}$$

where L, W and H are the length, width and height of the computational domain, respectively, N_x, N_y and N_z are the number of hexahedra in the x, y and z directions and N_p is the number of degrees of freedom per element when the polynomial degree is equal to p. In table 2 we present the values of N_x, N_y and N_z for the DNS. Following equations (15), the resolutions employed in the different directions for the DNS at $Re = 3000$ and for the (under-resolved) DNS at Reynolds $Re = 6000$ are given by:

$$\Delta_x^{DNS} = 0.006, \quad \Delta_y^{DNS} = 0.004, \quad \Delta_z^{DNS} = 0.004. \tag{16}$$

In table 1 the total number of degrees of freedom associated to the DNS is presented. The total number of DOFs employed for the DNS at Reynolds $Re = 3000$ is of the same order of magnitude as the one employed in [21] for the $med - res1$ simulation, realized with approximately 5000000 DOFs. In [21], two more resolved simulations, denoted by $med - res2$ and $high - res$, respectively, were also realized, but the authors stressed that the results of the three simulations were quite similar to each other. As a consequence we have decided to perform a simulation with a spatial resolution comparable to the $med - res1$ simulation. The total number of degrees of freedom for the DNS at Reynolds $Re = 6000$ is the same as the one for the DNS at $Re = 3000$: this implies that, for $Re = 6000$, we have, in principle, an underresolved DNS.

The equivalent grid spacings of equation (16) are compared to the Kolmogorov length scale in order to evaluate if the DNS we are performing are well resolved. The dimensional form of the Kolmogorov length scale can be estimated as follows:

$$\eta^* = \left(\frac{\nu^{*3}}{\epsilon^*} \right)^{\frac{1}{4}}, \tag{17}$$

Table 2: Number of hexahedra in the x, y, z directions associated to the DNS and the LES.

	$Re = 3000$	$Re = 6000$
DNS	$N_x = 56$, $N_y = 18$, $N_z = 18$	$N_x = 56$, $N_y = 18$, $N_z = 18$
LES	$N_x = 15$, $N_y = 5$, $N_z = 5$	$N_x = 23$, $N_y = 8$, $N_z = 8$

where ν^* is the dimensional kinematic viscosity and ϵ^* is the dimensional kinetic energy dissipation. Following [21], we define the kinetic energy dissipation as:

$$\epsilon^* = \frac{c{u_0^*}^3}{H^*}, \tag{18}$$

where c is a constant which, in most cases, assumes values in the interval $[0.6, 0.8]$, u_0^* is a characteristic velocity and H^* is a characteristic length. In [21], the characteristic velocity is set equal to the velocity of the gravity current head as:

$$u_0^* = \frac{1}{2}\sqrt{\frac{g^*(\rho_1^* - \rho_2^*)H^*}{\rho_2^*}},$$

where ρ_1^* and ρ_2^*, with $\rho_1^* > \rho_2^*$, are the dimensional densities on the left and on the right of the initial discontinuity. The non-dimensionalization is carried out in the present work using the buoyancy velocity u_b^* defined in equation (6). As a consequence, u_0^* can be rewritten as:

$$u_0^* = \frac{1}{2}\sqrt{\frac{\rho_1^*}{\rho_2^*}}u_b^* = \frac{1}{2}\sqrt{\frac{\rho_1}{\rho_2}}u_b^*. \tag{19}$$

Rewriting equation (17) employing equations (18) and (19) and simplifying, we get for the non-dimensional Kolmogorov length scale:

$$\eta = \left(\frac{\nu^3}{\frac{c}{8(\sqrt{\gamma_r})^3}}\right)^{\frac{1}{4}}, \tag{20}$$

where, as before, $\gamma_r = \rho_2/\rho_1$. For the kinematic viscosity, Sutherland's law is employed, obtaining:

$$\nu = \frac{T^\alpha}{\rho Re}. \tag{21}$$

As a result we obtain the following values:

$$\eta_{3000} = 0.004, \quad \eta_{6000} = 0.002. \tag{22}$$

If we compare the employed resolutions of equation (16) with the non dimensional Kolmogorov length scales of the previous equation, we can claim from this estimate that the DNS at $Re = 3000$ is quite well resolved, while the simulation at $Re = 6000$ is under-resolved.

Considering the $Re = 3000$ DNS, in an early stage of the simulation ($t = 2.9$) Kelvin Helmholtz rolls develop at the interface between the light and

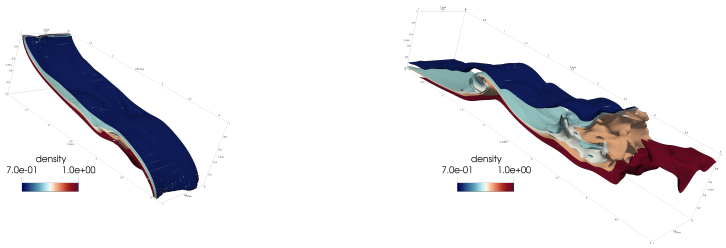

(a) (b)

Fig. 2: DNS density isosurfaces ($\rho = 0.72, 0.82, 0.85, 0.88, 0.98$) for $Re = 3000$, at $t = 2.9$ (left) and $t = 8.7$ (right).

the dense fronts and are clearly distinguishable (see the density isocontours represented in figure 2(a)). As also pointed out in [5] for the two-dimensional case, a typical feature of non-Boussinesq density currents is evident in this early phase of the simulation: instabilities at the interfacial region between the light and the dense fluid evolve more rapidly in correspondence to the rightward moving dense front with respect to the left propagating light front (see figure 2(a)). This happens because the velocity difference and the shear are larger, leading to a greater destabilizing effect. This non-symmetric pattern is absent in Boussinesq simulations: examining for example figure 1-b in [21], we can see that the two-dimensional Kelvin Helmholtz rolls develop in a symmetric way with respect to the position of the initial discontinuity.

Another noticeable difference between our non-Boussinesq simulation and the Boussinesq simulation in [21] is that, in the non-Boussinesq case, less turbulent structures are present, even if the same Reynolds number ($Re = 3000$) is considered: the larger density difference leads to a greater stratification and a consequent damping of turbulence (compare figures 2(a) and 2(b) with the corresponding figures 1-b and 1-c in [21]).

The last remark suggests us that, in the non-Boussinesq case, less spatial resolution could be sufficient in order to perform a DNS. In order to verify this hypothesis, we realize, for both $Re = 3000$ and $Re = 6000$, two additional simulations (denoted as DNS50) with a halved number of DOFs with respect to the DNS (see table 1). The dissipated energy and ΔRPE profiles provided by the DNS50 simulations show good agreement with the DNS results for both $Re = 3000$ and $Re = 6000$ (see figures 3(a) and 3(b)). In figure 3(b), we report also the ΔRPE curves obtained in [21] in correspondence to the high-res, med-res1 and med-res2 simulations. Since the authors affirm that convergence has been reached in their case, we can claim the same also for our $Re = 6000$ and $Re = 3000$ simulations, since even less differences are present between DNS and DNS50 in terms of ΔRPE.

In order to further support this conclusion we present, in figures 4(a) and 4(b), the TKE and mean streamwise velocity profiles, at $x = 2.5$ in the $Re =$

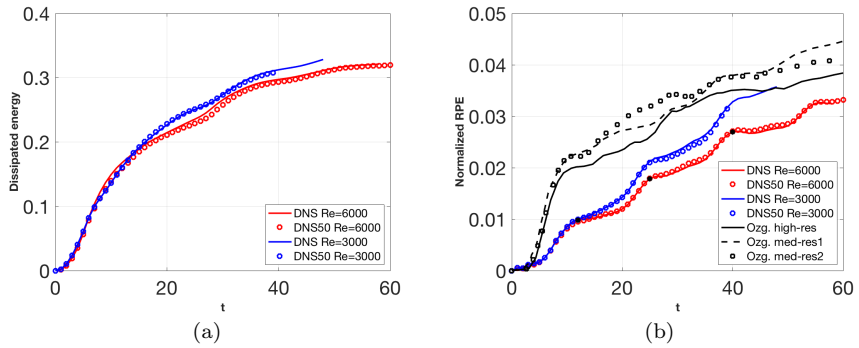

(a) (b)

Fig. 3: (a) Dissipated energy (b) Normalized Reference Potential Energy (ΔRPE) as a function of time for the DNS (solid line) and the DNS50 simulation (circles) and for Reynolds numbers $Re = 3000$ (blue) and $Re = 6000$ (red). In (b) also the ΔRPE curves obtained in [21] for $Re = 3000$ and in the Boussinesq case are represented in black.

6000 case, for $t \in [9, 16]$. DNS and DNS50 provide very similar results, even if some differences can be noticed. It should however be considered that the profiles are obtained by averaging only along the z direction, which is the only periodicity direction in our setting and that, as a consequence, a slight variability in the considered quantities is normal, even for a well resolved simulation. Notice also that similar conclusions can be reached considering different time intervals and x locations (not shown). Even if the estimates (22) indicate that the $Re = 6000$ simulation is under-resolved, considering the flow complexity and the fact that the Kolmogorov length scale has a statistical meaning, we trust more the conclusions we can draw comparing DNS and DNS50 simulations, since different diagnostics, both global (dissipated energy and RPE) and local (mean streamwise velocity, TKE) are carefully evaluated.

The density and $Q-$criterion fields for $Re = 6000$ (figure 5) show that the time interval taken into consideration allows to capture different phases of the flow evolution. After the current hits the lateral walls at $x = 0$ and $x = 5$, many three-dimensional turbulent structures and hairpin vortices are present and the flow loses the two-dimensional character (figures 5(a), 5(b)), due to three-dimensional convective instability for which the streamwise vortices stretch the spanwise vorticity concentrated in the Kelvin Helmholtz rolls. As time passes, turbulent activity reduces: in figures 5(c) and 5(d) and in 5(e) and 5(f) we observe a progressively reduced number and increased dimension of turbulent structures.

In addition to the general flow evolution just described, we can notice, looking at figures 4(a) and 4(b), a finer pattern. In particular we observe a reduction of the TKE in correspondence to the tilting of the mean streamwise velocity profile. The tilting of the mean streamwise velocity profile, and the reduction of the TKE, take place periodically during the simulation, in association to the encounter of the gravity current with the lateral walls at $x = 0$

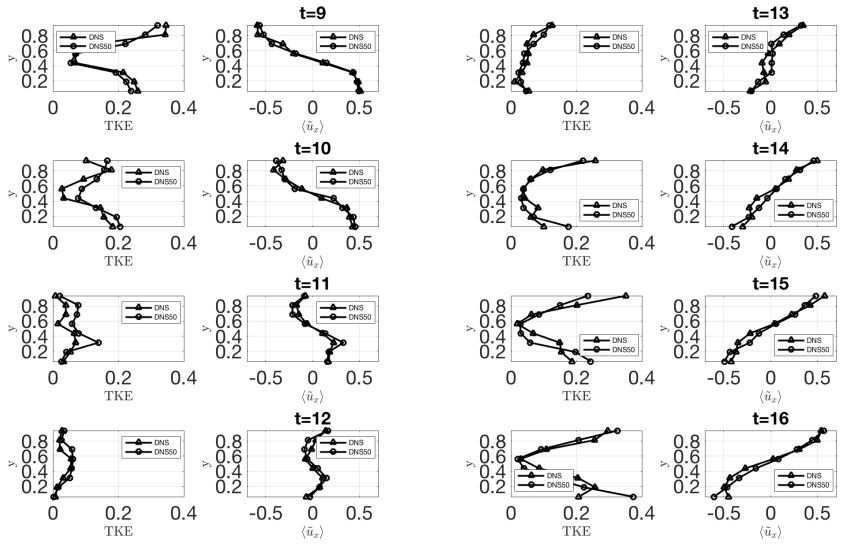

(a) (b)

Fig. 4: TKE and mean streamwise velocity $\langle \widetilde{u}_x \rangle$ profiles, at $x = 2.5$, for $Re = 6000$ and for $t \in [9, 16]$.

and $x = 5$. This periodic pattern has an impact also on the time evolution of the ΔRPE. In figure 3(b), we mark with an asterisk on the ΔRPE curve for $Re = 6000$ the instants of time at which the tilting of the mean streawise velocity profile is detected: we can notice that these points in time are almost evenly spaced and that, in correspondence to the same instants of time, we detect a reduction in the mixing rate represented by the reduced slope of the ΔRPE curve. Even if less evident with respect to the reduction of the TKE, also a reduction of the components $\langle \widetilde{u}'_x \widetilde{u}'_y \rangle$ and $\langle \widetilde{u}'_x \widetilde{u}'_z \rangle$ of the turbulent stresses can be observed (figures 6(a) and 6(b)).

5 Results of the LES experiments

In this section, the main results obtained from the LES experiments are presented and assessed in comparison to the corresponding DNS.

In table 1, the number of degrees of freedom associated to the different LES is presented. The number of degrees of freedom of the LES at $Re = 3000$ is of the same order of magnitude as the one employed in [21] for LES at the same Reynolds number (more precisely, it is similar to the number of DOFs employed for the low-res2 simulation in [21]). Following [24], the number of

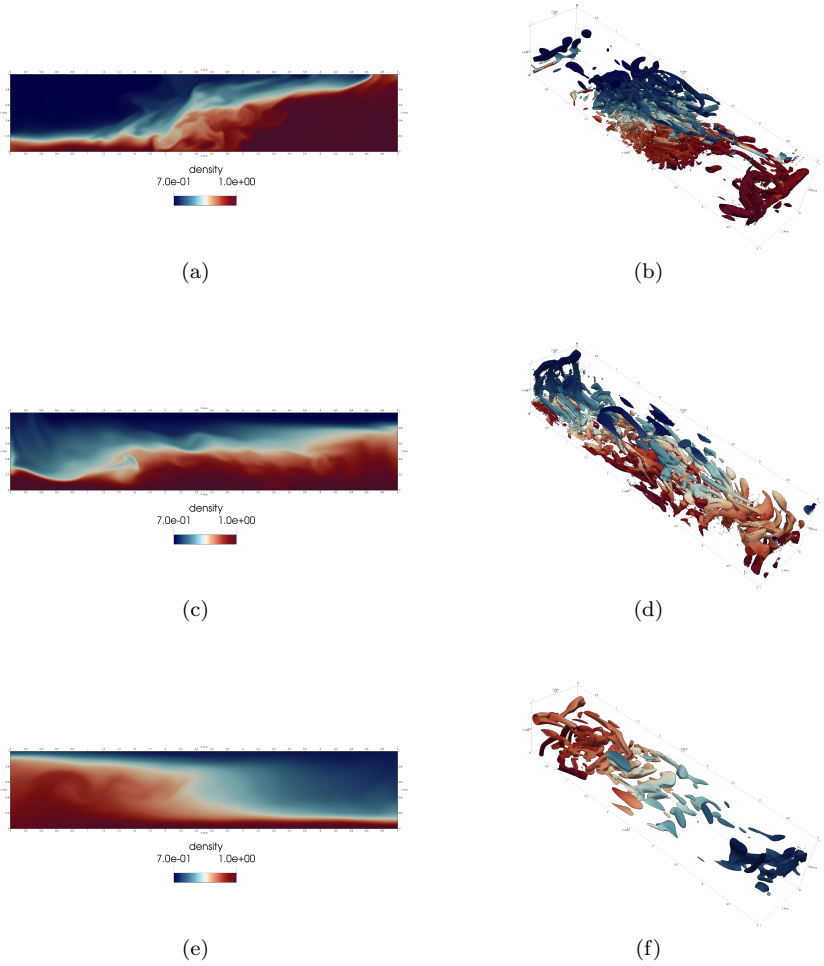

Fig. 5: Left: DNS density field (slice at $z = 0.5$). Right: DNS $Q = 0.01$ isosurface (colored by density) at $t = 15, 35, 55$ from top to bottom.

DOFs for the LES at $Re = 6000$ was obtained from the number of DOFs associated to the $Re = 3000$ LES as $N_{dofs}^{6000} = 2^{\frac{9}{4}} N_{dofs}^{3000}$.

As for the DNS, the computational grid was built starting from a structured hexahedral mesh. The number of hexahedra in each spatial direction, N_x, N_y and N_z, is presented in table 2.

In table 3 we report the computational cost for the different simulations in terms of CPU hours. We can notice that the cost of the different LES is from two to three orders of magnitude smaller than the cost of the corresponding DNS. The use of a turbulence model leads to an increase of the cost with respect to the corresponding no-model simulation, ranging from an increase of

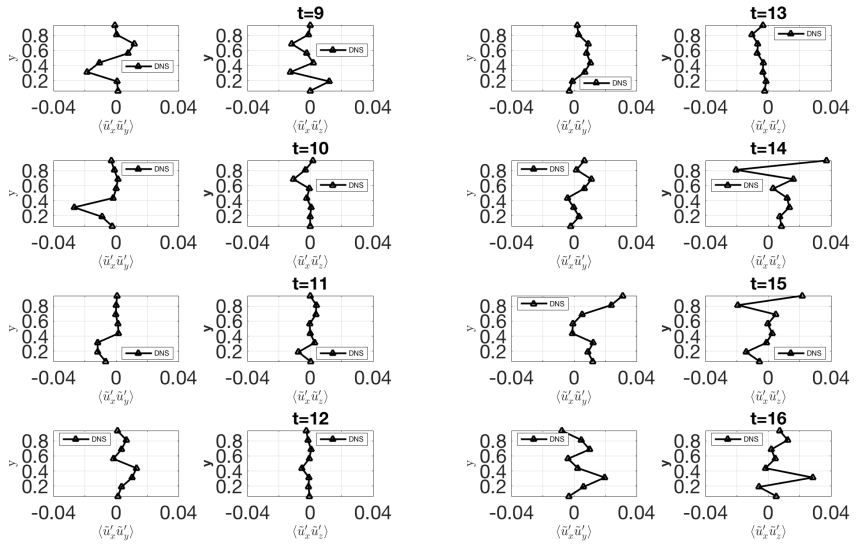

(a) (b)

Fig. 6: Turbulent stresses $\langle \widetilde{u}'_x \widetilde{u}'_y \rangle$ and $\langle \widetilde{u}'_x \widetilde{u}'_z \rangle$ profiles, at $x = 2.5$, for $Re = 6000$ and for $t \in [9, 16]$

Table 3: Computational cost (CPU hours) for the different simulations.

	$Re = 3000$	$Re = 6000$
DNS	133900	133900
No model	750	5400
Smagorinsky	875	6300
Isotropic dyn.	1115	7800
Anisotropic dyn.	1117	7800

16% for the Smagorinsky model to an increase of 50% for the dynamic models . All the simulations have been performed on the Marconi cluster at CINECA. 576 cores have been employed for DNS and for the LES at $Re = 6000$, while 288 cores have been employed for the LES at $Re = 3000$.

Even if the purpose of the present work is to find possible advantages of explicit dynamic (isotropic and anisotropic) turbulence models with respect to an implicit LES approach, we realize also an LES with the Smagorinsky model, due to its widespread use. We are aware of the fact that employing the Smagorinsky model in a transitional regime (like the one which characterizes the first phase of the lock-exchange evolution) could lead to an inaccurate solution also for more advanced points in time. For this reason and since we know that the Smagorinsky model could be very sensitive to the choice of the

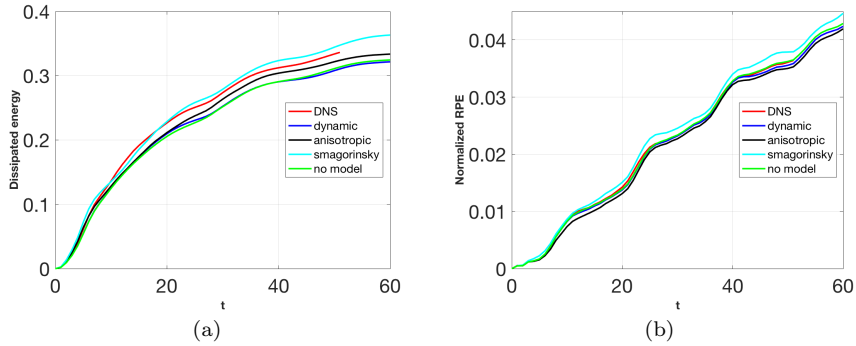

(a) (b)

Fig. 7: (a) Dissipated energy (b) Normalized Reference Potential Energy (ΔRPE) as a function of time, for $Re = 3000$.

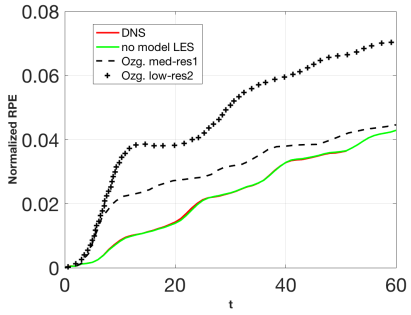

Fig. 8: Normalized Reference Potential Energy (ΔRPE) as a function of time, for $Re = 3000$.

Smagorinsky constant, in the $Re = 6000$ case, and as already performed in [21] for the Boussinesq regime, we test two different values ($C_s = 0.05, 0.1$) for the Smagorinsky constant (see also [10]).

In order to try to discriminate the behaviour of the different LES models and their performances with respect to the DNS results, we consider the dissipated energy profiles and the normalized Reference Potential Energy profiles as a function of time. The dissipated energy is computed as in equation (9).

Considering the $Re = 3000$ case and the time evolution of ΔRPE (figure 7(b)), very few differences are present between the LES and the DNS in reproducing the time evolution of stratified mixing. Only the Smagorinsky model ($C_s = 0.1$) clearly overestimates ΔRPE. The almost indistinguishable behaviour of DNS and no-model LES further support our conclusion that the non-Boussinesq regime is far less turbulent with respect to the Boussinesq one at the same Reynolds number: if we compare the mes-res1 and the low-res2 ΔRPE curves obtained in [21] and reported in figure 8, we notice far larger differences between them with respect to the almost negligible differences between our DNS and no-model LES at the same Reynolds number.

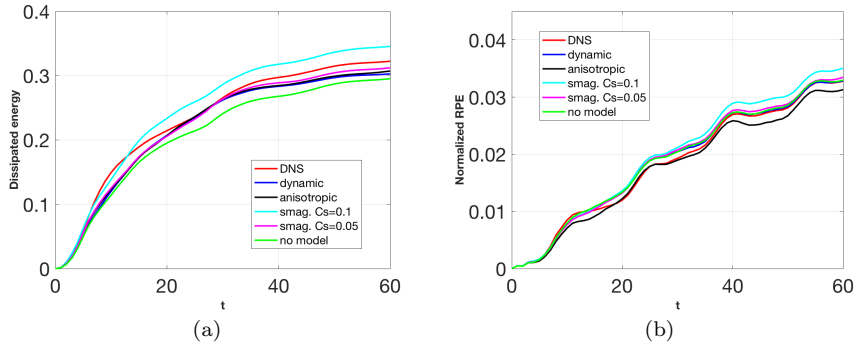

(a) (b)

Fig. 9: (a) Dissipated energy (b) Normalized Reference Potential Energy (ΔRPE) as a function of time, for $Re = 6000$.

The dissipated energy profiles (figure 7(a)) present slightly more evident differences. While the isotropic dynamic model and the no-model dissipated energy profiles are almost indistinguishable, the anisotropic dynamic model is more dissipative, becoming the closer one to the DNS profile. Also the Smagorinsky model ($C_s = 0.1$) is quite closer to the DNS at the beginning of the simulation, even if, towards the end of the simulation, it introduces too much dissipation.

Moving to the more interesting $Re = 6000$ case, we can appreciate more discrepancies between the DNS and the LES realized with different turbulence models for both the normalized RPE and the dissipated energy. Concerning the ΔRPE evolution, none of the LES is able to correctly reproduce the behaviour of the DNS ΔRPE over the whole simulation time. The anisotropic dynamic model provides better results in a first phase of the simulation, for $t \in [15, 35]$, while the isotropic dynamic model, no-model and Smagorinsky model ($C_s = 0.05$), whose behaviour in terms of ΔRPE is comparable, better reproduce the DNS ΔRPE curve towards the end of the simulation, for $t \in [35, 60]$. Concerning the dissipated energy evolution, the behaviour of the isotropic dynamic, anisotropic dynamic and Smagorinsky ($C_s = 0.05$) models is almost the same, and the more similar to the DNS one. The excessively dissipative character of the Smagorinsky model with $C_s = 0.1$ is even more evident than in the $Re = 3000$ case. Together with the excessive dissipation, the Smagorinsky model with $C_s = 0.1$ also overestimates the normalized RPE: this can be explained by the fact that bigger and more coherent turbulent structures are maintained, entailing an increased rate of stratified mixing [21] (figure 10).

In order to better understand the spatial distribution of the subgrid-scale dissipation introduced by the different turbulence models, in figure 11, which refers to the $Re = 6000$ simulation at $t = 35$, we represent the term $-\tau_{ij}\partial_j\widetilde{u}_i$ evaluated over a slice located at $z = 0.5$. This analysis allows to show that the subgrid-scale dissipation introduced by the Smagorinsky model ($C_s = 0.1$) involves a larger part of the domain with respect to the isotropic dynamic model, for which a very small portion of the domain presents values for the

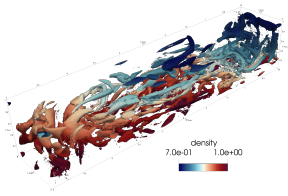

(a) DNS

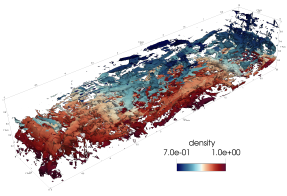

(b) No model

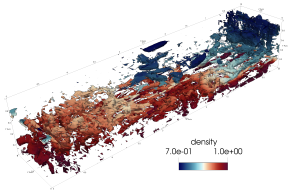

(c) Isotropic dynamic model

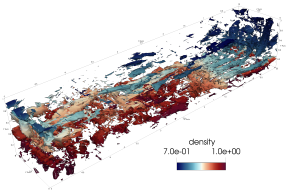

(d) Anisotropic dynamic model

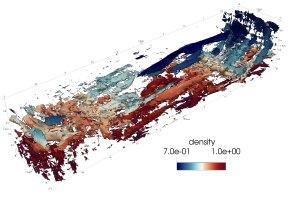

(e) Smagorinsky model $C_s = 0.1$

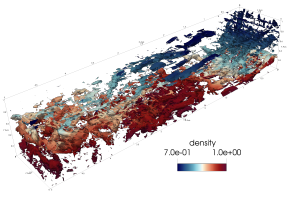

(f) Smagorinsky model $C_s = 0.05$

Fig. 10: $Q = 0.01$ isosurface (colored by density) at $t = 35$ for $Re = 6000$.

subgrid-scale dissipation which are different from zero. On the other hand, the anisotropic dynamic model introduces the subgrid scale dissipation following a quite scattered pattern, with the presence of consistent backscattering (negative values for the subgrid-scale dissipation). Notice that the presence of consistent backscatter in shear layers has already been highlighted for example in [23]. The same scattered pattern for the subgrid-scale dissipation and backscattering are present also for more advanced instant of time, even if smaller absolute values of the subgrid-scale dissipation are detected (not shown). This could be the explanation of the behaviour of the anisotropic dynamic model in terms of ΔRPE. The pattern of the subgrid-scale dissipation and backscatter provided by the anisotropic dynamic model appear to have a positive impact on the reproduction of the rate of stratified mixing in an intermediate phase of the simulation, when the turbulent activity is more pro-

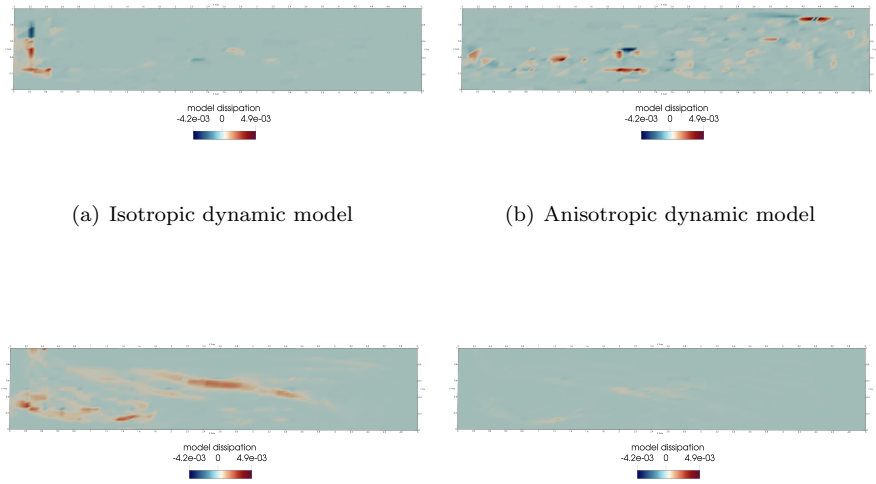

(a) Isotropic dynamic model

(b) Anisotropic dynamic model

(c) Smagorinsky model $C_s = 0.1$

(d) Smagorinsky model $C_s = 0.05$

Fig. 11: Subgrid-scale dissipation $\tau_{ij}\partial_j\widetilde{u}_i$ evaluated over the slice $z = 0.5$, at $t = 35$ for $Re = 6000$.

nounced and when the dimension of the turbulent structures is smaller (see figure 5). On the other hand, in the last phase of the simulation, the scattered pattern of the subgrid-scale dissipation and the backscatter could have an excessive impact in disrupting the coherence of turbulent structures, thus leading to reduction of the rate of stratified mixing with respect to the DNS (see figure 9(b)). Concerning the Smagorinsky model with $C_s = 0.05$, the pattern of the introduced subgrid scale dissipation is similar to that obtained with $C_s = 0.1$, but the values for the introduced subgrid-scale dissipation are smaller.

Drawing some conclusions, the present LES analysis provides a first indication about the superiority of dynamic models with respect to an implicit LES approach, in the context of gravity currents simulation with a Discontinuous Galerkin method. Results comparable to the ones provided by dynamic models can be obtained also using the Smagorinky model even if, as expected, in the present transitional regime a careful choice of the Smagorisnky constant is necessary. However, in the present non-Boussinesq regime and with the Reynolds numbers we have considered, the differences between DSN and no model LES is still too reduced (in particular if compared with the differences which are found in the Boussinesq regime for the normalized RPE) to be able to obtain a firm conclusion about the superiority of explicit LES with respect to an implicit LES approach.

6 Conclusions and future perspectives

We have carried out three-dimensional DNS and LES of non-Boussinesq gravity currents in the lock-exchange configuration. First, three-dimensional DNS in the non-Boussinesq regime were performed at two different Reynolds numbers ($Re = 3000$, $Re = 6000$).

Some differences between our non-Boussinesq simulations and the Boussinesq results at $Re = 3000$ in [21] have been highlighted. In particular, in our case, there is a non symmetric development of the Kelvin-Helmholtz billows with respect to the position of the initial discontinuity. Moreover, due to the greater stratification, less turbulent structures are present than in the corresponding Boussinesq simulation. In addition to these remarks, a periodic pattern has been identified analyzing the DNS in terms of TKE, turbulent stresses, mean velocities and Reference Potential Energy: the successive encounters of the gravity currents with the lateral walls cause a periodic inversion of the mean streamwise velocity profile associated to a reduction of the TKE and of the rate of stratified mixing.

In the LES experiments we have compared the Smagorinsky model ($C_s = 0.05, 0.1$), the isotropic dynamic model and the anisotropic dynamic model, together with a no model run. The considered diagnostics (instantaneous density and Q-criterion fields, time evolution of the dissipated energy and of the Reference Potential Energy) provide a first indication about the superiority of dynamic models with respect to the no-model LES. Also the Smagorisnky model is able to provide results comparable to the ones obtained with dynamic models and better than the no-model results: it however requires, in the present transitional regime, the introduction of ad hoc values for the Smagorinsky constant, which we think it is a serious drawback.

In spite of these remarks, we are aware of the fact that the results provided by the different turbulence models are still quite similar between each other for the investigated non-Boussinesq regime. This is also due to the fact that we have considered Reynolds numbers typically explored in the Boussinesq regime [21], where less stratification is present and more turbulent structures are able to develop. As a consequence we are planning to perform simulations at higher Reynolds numbers in order to better highlight the differences in the performances of the tested turbulence models.

From the turbulence modeling perspective, another main goal is the implementation of new turbulence models for variable density flows, based on the work [13], in the same configuration as employed for the LES carried out here, in order to see if an improvement of the results can be obtained with respect to the results obtained with the turbulence models already tested.

Acknowledgements

This paper contains some revised and extended results from the first author's PhD thesis work. We would like to acknowledge the careful and constructive

remarks by two anonymous reviewers, which have helped in improving the clarity of the paper. We are happy to acknowledge the continuous help of M. Restelli and M.Tugnoli with the application of the FEMILARO code. The results of this research have been achieved using the computational resources made available at CINECA (Italy) by the LISA high performance computing project *DECLES: Large Eddy Simulation of Density Currents and Variable Density Flows, HPL13PJ6YS*.

References

1. Abbà, A., Bonaventura, L., Nini, M., Restelli, M.: Dynamic models for Large Eddy Simulation of compressible flows with a high order DG method. Computers & Fluids **122**, 209–222 (2015)
2. Abbà, A., Cercignani, C., Valdettaro, L.: Analysis of Subgrid Scale Models. Computer and Mathematics with Applications **46**, 521–535 (2003)
3. Bassi, F., Rebay, S.: High Order Accurate Discontinuous Finite Element Method for the Numerical Solution of the Compressible Navier-Stokes Equations. Journal of Computational Physics **131**, 267–279 (1997)
4. Berselli, L., Fischer, P., Iliescu, T., Özgökmen, T.: Horizontal Large Eddy Simulation of Stratified Mixing in a Lock-Exchange System. Journal of Scientific Computing **49**, 3–20 (2011)
5. Birman, V.K., Martin, J., Meiburg, E.: The non-Boussinesq Lock-exchange problem. Part 2. High-resolution simulations. Journal of Fluid Mechanics **537**, 125–144 (2005)
6. Van der Bos, F., Van der Vegt, J., Geurts, B.: A multi-scale formulation for compressible turbulent flows suitable for general variational discretization techniques. Computer Methods in Applied Mechanics and Engineering **196**, 2863–2875 (2007)
7. C.Bassi: Large Eddy Simulation of compressible variable density flows with a high-order DG-LES model. Ph.D. thesis, Politecnico di Milano (2018)
8. C.Bassi, Abbà, A., Bonaventura, L., Valdettaro, L.: Large Eddy Simulation of gravity currents with a high-order DG method. Communications in Applied and Industrial Mathematics **8**, 128–148 (2017)
9. Cockburn, B., Shu, C.: The Local Discontinuous Galerkin Method for Time-Dependent Convection Diffusion Systems. SIAM Journal of Numerical Analysis **35**, 2440–2463 (1998)
10. Ferziger, J.: Direct and large-eddy simulation of turbulence. In: H. Baumert, J. Simpson, J. Sündermann (eds.) Marine Turbulence - Theories, Observations and Models, pp. 160–181. Cambridge University Press (2005)
11. Garnier, E., Adams, N., Sagaut, P.: Large Eddy Simulation for Compressible Flows. Springer Verlag (2009)
12. Germano, M.: Turbulence: the filtering approach. Journal of Fluid Mechanics **238**, 325–336 (1992)
13. Germano, M., Abbà, A., Arina, R., Bonaventura, L.: On the extension of the eddy viscosity model to compressible flows. Physics of Fluids **26**, 041702 (2014)
14. Germano, M., Piomelli, U., Moin, P., Cabot, W.: A Dynamic Subgrid-Scale Eddy Viscosity Model. Physics of Fluids **3(7)**, 1760–1765 (1991)
15. Gill, A.: Atmosphere-Ocean Dynamics. Academic Press (1982)
16. Härtel, C., Meiburg, E., Necker, F.: Analysis and direct numerical simulation of the flow at a gravity-current head. Part 1. Flow topology and front speed for slip and no-slip boundaries. Journal of Fluid Mechanics **418**, 189–212 (2000)
17. Hughes, T., Mazzei, L., Oberai, A.: Large Eddy Simulation of turbulent channel flows by the variational multiscale method. Physics of Fluids **13**, 1784–1799 (2001)
18. Hunt, J., Wray, A., Moin, P.: Eddies, stream, and convergence zones in turbulent flows. Tech. Rep. CTR-S88, Center for Turbulence Research (1988)
19. John, V., Kindl, A.: Numerical studies of finite element Variational Multiscale Methods for turbulent flow simulations. Computer Methods in Applied Mechanics and Engineering **199**, 841–852 (2010)

20. Kirby, R., Karniadakis, G.: De-aliasing on non-uniform grids: algorithms and applications. Journal of Computational Physics **191**, 249–264 (2003)
21. Özgökmen, T., Iliescu, T., Fischer, P.: Large Eddy Simulation of stratified mixing in a three-dimensional Lock-exchange system. Ocean Modelling **26**, 134–155 (2009)
22. Özgökmen, T., Iliescu, T., Fischer, P., Srinivasan, A., Duan, J.: Large Eddy Simulation of stratified mixing in two-dimensional dam-break problem in a rectangular enclosed domain. Ocean Modelling **16**, 106–140 (2007)
23. Piomelli, U., Cabot, W., Moin, P., Lee, S.: Subgrid -scale backscatter in turbulent and transitional flows. Physics of Fluids **3**, 1766–1771 (1991)
24. Sagaut, P.: Large Eddy Simulation for Incompressible Flows: An Introduction. Springer Verlag (2006)
25. Simpson, J.: Gravity currents in the environment and in the laboratory. Cambridge University Press (1997)
26. Smagorinsky, J., Manabe, S., Holloway, J.L.: Numerical results from a nine-level general circulation model of the atmosphere. Monthly Weather Review **93**, 727–768 (1965)
27. Spiteri, R., Ruuth, S.: A new class of optimal high-order Strong Stability Preserving time discretization methods. SIAM Journal of Numerical Analysis **40**, 469–491 (2002)
28. Toro, E.: Riemann Solvers and Numerical Methods for Fluid Dynamics, a Practical Introduction. Springer (2009)
29. Tseng, Y., Ferziger, J.: Mixing and available potential energy in stratified flows. Physics of Fluids **13**, 1281–1293 (2001)
30. Tugnoli, M., A.Abbà, Bonaventura, L., Restelli, M.: A locally p-adaptive approach for Large Eddy Simulation of compressible flows in a DG framework. Journal of Computational Physics **349**, 33–58 (2017)
31. Winters, K., Lombard, P., Riley, J., D'Asaro, E.: Available potential energy and mixing in density-stratified fluids. Journal of Fluid Mechanics **289**, 115–128 (1995)